

## Article

# Fluorescent Phthalocyanine-Encapsulated Bovine Serum Albumin Nanoparticles: Their Deployment as Therapeutic Agents in the NIR Region

Raluca Borlan <sup>1,2</sup>, Daria Stoia <sup>2</sup>, Luiza Gaina <sup>3</sup>, Andreea Campu <sup>2</sup>, Gabriel Marc <sup>4</sup>, Maria Perde-Schrepler <sup>5</sup>, Mihaela Silion <sup>6</sup>, Dana Maniu <sup>1,2</sup>, Monica Focsan <sup>2,\*</sup> and Simion Astilean <sup>1,2,\*</sup>

- <sup>1</sup> Biomolecular Physics Department, Faculty of Physics, Babes-Bolyai University, 400084 Cluj-Napoca, Romania; raluca.borlan@ubbcluj.ro (R.B.); dana.maniu@ubbcluj.ro (D.M.)
  - <sup>2</sup> Nanobiophotonics and Laser Microspectroscopy Centre, Interdisciplinary Research Institute on Bio-Nano-Sciences, Babes-Bolyai University, 400271 Cluj-Napoca, Romania; daria.stoia@stud.ubbcluj.ro (D.S.); andreea.campu@ubbcluj.ro (A.C.)
  - <sup>3</sup> The Research Centre on Fundamental and Applied Heterochemistry, Department of Chemistry, Faculty of Chemistry and Chemical Engineering, Babes-Bolyai University, 400028 Cluj-Napoca, Romania; ioana.gaina@ubbcluj.ro
  - <sup>4</sup> Department of Pharmaceutical Chemistry, Faculty of Pharmacy, 'Iuliu Hațieganu' University of Medicine and Pharmacy, 41 Victor Babes Street, 400012 Cluj-Napoca, Romania; marc.gabriel@umfcluj.ro
  - <sup>5</sup> Department of Radiobiology and Tumor Biology, Oncology Institute Prof. Dr. Ion Chiricuta, 400015 Cluj-Napoca, Romania; pmariaida@yahoo.com
  - <sup>6</sup> Physics of Polymers and Polymeric Materials, "Petru Poni" Institute of Macromolecular Chemistry, Romanian Academy, 700487 Iasi, Romania; silion.mihaela@icmpp.ro
- \* Correspondence: monica.iosin@ubbcluj.ro (M.F.); simion.astilean@ubbcluj.ro (S.A.)



**Citation:** Borlan, R.; Stoia, D.; Gaina, L.; Campu, A.; Marc, G.; Perde-Schrepler, M.; Silion, M.; Maniu, D.; Focsan, M.; Astilean, S. Fluorescent Phthalocyanine-Encapsulated Bovine Serum Albumin Nanoparticles: Their Deployment as Therapeutic Agents in the NIR Region. *Molecules* **2021**, *26*, 4679. <https://doi.org/10.3390/molecules26154679>

Academic Editor: Josef Jampilek

Received: 30 June 2021

Accepted: 28 July 2021

Published: 2 August 2021

**Publisher's Note:** MDPI stays neutral with regard to jurisdictional claims in published maps and institutional affiliations.



**Copyright:** © 2021 by the authors. Licensee MDPI, Basel, Switzerland. This article is an open access article distributed under the terms and conditions of the Creative Commons Attribution (CC BY) license (<https://creativecommons.org/licenses/by/4.0/>).

**Abstract:** In recent times, researchers have aimed for new strategies to combat cancer by the implementation of nanotechnologies in biomedical applications. This work focuses on developing protein-based nanoparticles loaded with a newly synthesized NIR emitting and absorbing phthalocyanine dye, with photodynamic and photothermal properties. More precisely, we synthesized highly reproducible bovine serum albumin-based nanoparticles (75% particle yield) through a two-step protocol and successfully encapsulated the NIR active photosensitizer agent, achieving a good loading efficiency of 91%. Making use of molecular docking simulations, we confirm that the NIR photosensitizer is well protected within the nanoparticles, docked in site I of the albumin molecule. Encouraging results were obtained for our nanoparticles towards biomedical use, thanks to their negatively charged surface ( $-13.6 \pm 0.5$  mV) and hydrodynamic diameter ( $25.06 \pm 0.62$  nm), favorable for benefitting from the enhanced permeability and retention effect; moreover, the MTT viability assay upholds the good biocompatibility of our NIR active nanoparticles. Finally, upon irradiation with an NIR 785 nm laser, the dual phototherapeutic effect of our NIR fluorescent nanoparticles was highlighted by their excellent light-to-heat conversion performance (photothermal conversion efficiency 20%) and good photothermal and size stability, supporting their further implementation as fluorescent therapeutic agents in biomedical applications.

**Keywords:** NIR photoactive molecules; albumin-based nanoparticles; dual phototherapy; NIR fluorescent agents; ovarian cancer

## 1. Introduction

After heart disease, cancer is the second most frequent cause of death around the world, with over 4.5 million new cases and over 2 million deaths in 2018 [1]. Therefore, in the past decades, scientists have searched for new ways to fight against cancer, and the past years have brought huge progress in the field of nanotechnology, especially in the biomedical area. At present, researchers make use of nanotechnology in medical applications to develop nanoparticles (NPs) able to deliver contrast agents and other

substances of interest to tumor sites and, at the same time, tailored to fight cancer through different types of therapy [2,3]. For example, gold NPs have been developed together with indocyanine green in order to achieve a hybrid nano-system to perform both photodynamic and photothermal therapy for an innovative targeted and efficient therapeutic strategy [4].

An up-and-coming cancer treatment method is photodynamic therapy (PDT). For this therapy to work, three elements, namely a photosensitizer (PS) agent, PS specific excitation wavelength light, and intracellular oxygen, are indispensable. If we combine these three elements, they produce photochemical reactions that lead to the generation of cytotoxic reactive oxygen species, predominantly singlet oxygen ( $^1\text{O}_2$ ). This reactive oxygen species can trigger the patient's immune system, can close the vasculature around the tumor, and, most importantly, can cause immediate cancer cell death [5,6]. Champeau M. et al. explained that, in the dermatological field, PDT is implemented as a treatment for skin cancer; more specifically, most clinical trials use 5-aminolevulinic acid in high doses as a cream to cover the lesions [6]. After a predefined incubation period, the lesion is exposed to a laser, usually of 635 nm, to stimulate the PS agent. After the PS molecule is stimulated, PDT occurs.

Another cancer therapy that has potential to be translated to clinical use is photothermal therapy (PTT). This technique also implies the use of electromagnetic radiation, and, at present, the most used spectral domain for this type of therapy is the visible one. Aside from light, this therapy involves thermal agents that absorb and then convert light into heat when the electromagnetic radiation has a suitable wavelength. In biomedical applications, these thermal treatments rely on the local heating of the tissue or desired organ in a very specific time frame. In humans, temperature plays a very important role; thus, when the body temperature exceeds 37 °C, it is a sign of a cold, an infection, or another condition that could put our health in danger [7]. If the temperature rises above 42 °C [7], the cells from the targeted tissue will undergo necrosis, and if it reaches 60 °C [7], protein denaturation takes place instantly and is permanent. This kind of treatment is very efficient in theory, but, in real life, it presents significant drawbacks when using free thermal agents due to their lack of distinction between healthy and cancerous tissues [7–9]. Rajkumar et al. performed PTT combined with chemotherapy on cervical cancer cells, namely the HeLa cellular line, through loaded NPs with fluorescein isothiocyanate and doxorubicin [10]. For a more specific targeting of these cancer cells, the NPs were additionally functionalized with folic acid. After incubating HeLa cells with the NPs, the samples were irradiated for 5 min with a 532 nm laser that increased their temperature by 13 °C.

Despite the restraints encountered when exciting biological samples with light from the visible spectrum, such as low level of tissue penetration, currently, most medical applications use therapeutic and contrast agents that possess absorption and emission properties in the visible domain [11]. Therefore, to combat their drawbacks, in the past years, researchers have developed and implemented nano-sized agents in pre-clinical studies and clinical trials that are able to encapsulate photoactive molecules in the NIR domain. Unlike the ultraviolet and visible spectrum, NIR electromagnetic radiation penetrates the biological tissue deeper (500  $\mu\text{m}$  up to 1–2 cm) because fluids and biological tissue present a minimal absorption between 650–1400 nm, hereby acquiring the name *biological transparency window* [12]. Anna Oniszczuk et al. [13] claims that the most appropriate irradiation for the human body is with light that has a wavelength of 630 nm or above. However, despite the fact that the Food and Drug Administration has approved many fluorophores for medical use with emission properties in the ultraviolet and visible region of the electromagnetic spectrum, only two emit light in the NIR domain (650–900 nm), namely indocyanine green and methylene blue [4,14].

In recent years, dyes from the phthalocyanine family gained attention in biomedical research as contrast and therapeutic NIR agents. These synthetic dyes are made out of four isoindole units interconnected with nitrogen atoms, forming a large ring of 18  $\pi$  electrons, and were firstly synthesized in 1928 out of pure accident, but their efficacy as dyes and toners was established only in 1934. Phthalocyanines are usually used in various

fields, e.g., chemical sensors, intrinsic semiconductors, etc. and are thoroughly studied as photosensitive chemical compounds for PDT, thanks to their high photostability and good chemical and thermal stability. However, the use of free phthalocyanines in biological applications is limited because they are insoluble in water and therefore tend to create aggregates [15–17].

Based on the assumption that a functional dye must fulfil a series of requirements to be simultaneously a good NIR PS in PDT [18] and a fluorescent agent for NIR bio-imaging [19], for this study, the phthalocyanine derivatives were considered, being known as light-sensitive molecules having the absorption and emission maxima in the red/near IR region and a high level of absorption molar coefficient, respectively. The metal ion coordinated in the central cavity of the phthalocyanine plays an important role in the fluorescence emission, singlet oxygen generation, intersystem-crossing efficacy, energy and lifetime of the triplet state [20], and in solution aggregation behavior [21]. As shown by Tasso et al., the Zn(II) ion from zinc(II)phthalocyanine is one of the most efficient  $^1\text{O}_2$  producers and is able to enhance the fluorescence emission, and the intermolecular aggregation can be more easily disrupted in comparison with metalophthalocyanine containing Cu, Ni, Co, or Pd ions [20].

One promising product of nanotechnological advancements in therapeutic applications, detection, and visualization of cancerous tissues is NPs. They can be used as carriers for different PS, thermal, and contrast agents throughout the human body to cancerous cells, in order to eliminate all unwanted drawbacks and side effects of dispensing free agents, such as poor biocompatibility, low photostability, and non-specific targeting. Hereby, special consideration was given to protein NPs, being biodegradable, being biocompatible, and having a versatile chemical structure [22,23], especially albumin NPs. Albumin is the most abundant protein in plasma, able to encapsulate a wide range of dyes, drugs, PS agents, thermal agents, and other biologically active compounds [23,24], and, for commercial purposes, it can be derived from egg white, rat serum, bovine serum (BSA), and human serum. BSA's chemical structure is formed of 583 amino acids, having a molecular weight of 69.3 kDa, and, in the past years, NPs synthesized with this protein have been heavily tested in many preclinical studies [25,26]. Moreover, the dimension of BSA NPs can be controlled so that they are in the optimum domain to seize the enhanced permeability and retention effect (EPR).

In the current clinical context, where significant effort is invested in the development of new approaches for relevant medical applications, the purpose of this study is to design state-of-the-art contrast and therapeutic agents with optical features in the NIR region of the electromagnetic spectrum. The newly synthesized NIR fluorescent photoactive molecule, namely Zinc(II)-2,9,16,23-tetraamio-phthalocyanine (hereinafter denoted as phthaloNH<sub>2</sub>), able to synergistically combine photothermal and photodynamic therapeutic effects, has been selected for this study. Furthermore, for improved performance and a safe biomedical administration, we encapsulated, in a controlled manner, the NIR fluorophore within protein NPs. Using an adapted fabrication strategy [27], the phthaloNH<sub>2</sub>-loaded protein NPs were designed to meet the following requirements: they (i) present a high photoactive molecule loading capacity, (ii) present reproduction in synthesis, (iii) perform good therapeutic effects, (iv) are biocompatible, etc. PhthaloNH<sub>2</sub> is a dye in the family of phthalocyanines, able to act at the same time as a PS, and as thermal and contrast agent; the fine equilibrium between the three functions of the NIR molecule allows us to implement phthaloNH<sub>2</sub> as a multimodal therapeutic and contrast agent. The fluorescence capacity and in vitro biocompatibility of the phthaloNH<sub>2</sub> loaded BSA NPs (hereinafter denoted as BSA&phthaloNH<sub>2</sub> NPs) were successfully tested, foreseeing promising outcomes in future studies as an NIR contrast agent in the imaging of living cells. Moreover, even though the relation between the emissive properties, light-to-heat conversion, and  $^1\text{O}_2$  generation yields of the photoactive molecules changed once encapsulated within the BSA NPs, their potential to operate as dual therapeutic agents through the synergistic integration of photodynamic and photothermal properties on a single therapeutic agent

was evaluated, in this way creating a highly efficient nano-sized phototheranostic agent for cancer treatment.

## 2. Results

### 2.1. Optical Characterization of PhthaloNH<sub>2</sub>

Phthalocyanine synthesis implies a macrocyclization reaction, using starting materials which fall in two different categories: the first one which needs an extra source of nitrogen (phthalic acids, phthalic anhydrides, phthalimide) and the second one which does not necessarily need an external nitrogen source (phthalonitriles, isoindoline-1,3-diimine, 2-cyanobenzamide, phthalimide) and a metal halide or salt for metalated phthalocyanine, respectively. The best alternative for the preparation of Zn(II) tetraamine phthalocyanine [28,29] is the reduction of the nitro group of Zn(II) tetranitro phthalocyanine in the presence of disodium sulfide. The nitro precursor can be synthesized by tetracyclization of nitrophthalonitrile [30] or nitrophthalamide [28].

The newly synthesized phthaloNH<sub>2</sub> dye was obtained, briefly, from mixing Zinc(II) tetranitrophthalocyanine and Na<sub>2</sub>S·9H<sub>2</sub>O. After purification, the dye was further encapsulated in BSA-based NPs following a two-step procedure: (i) desolvation and (ii) cross-linking.

First, using UV-Vis-NIR absorbance (Figure 1a) and fluorescence spectroscopy (Figure 1b), we were able to characterize the photoactive agent in different solvent solutions, PBS and DMSO. Considering that the used photoactive agent is actually a predominantly hydrophobic molecule, we can easily observe from Figure 1 that phthaloNH<sub>2</sub> presents both absorbance and fluorescence properties only when dissolved in DMSO solution (blue spectra), showing an absorption maximum at 775 nm and an emission maximum at 796 nm. On the contrary, if dissolved in PBS solution (orange spectra), the absorbance spectrum aspect of the phthaloNH<sub>2</sub> is strongly modified, and the fluorescence emission is lost. Therefore, we can conclude that to preserve phthaloNH<sub>2</sub>s properties, we need to dissolve it only in aprotic polar solvents, specifically the highly polar DMSO. Thus, for the photoactive molecule to maintain its phototheranostic properties under physiological conditions, and for a safe in vivo administration, the encapsulation of the NIR dye within biocompatible nano-carriers is recommended, i.e., protein-based NPs.

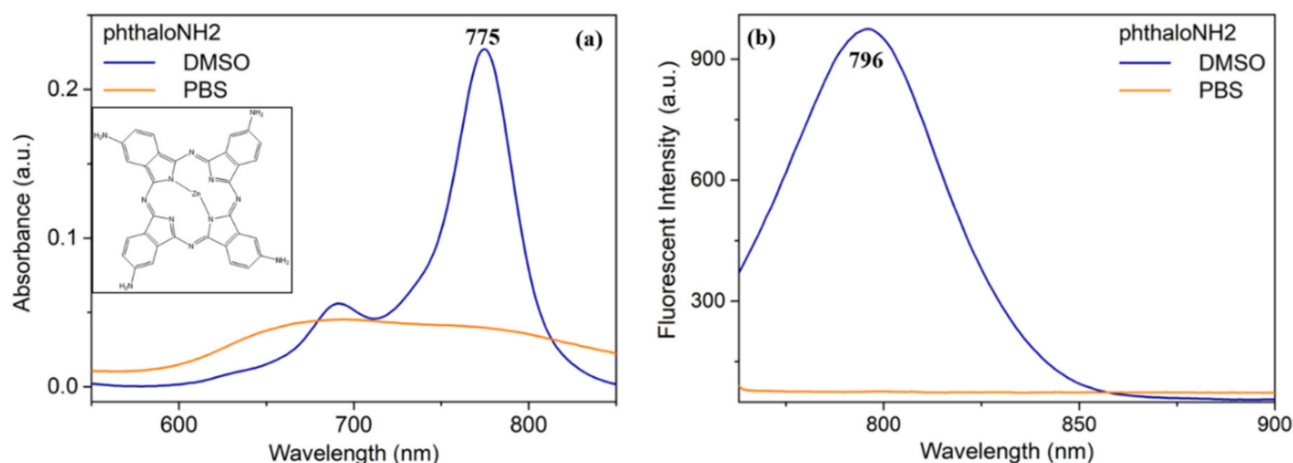


**Figure 1.** Absorbance (a) and fluorescence emission (b) spectra of the free phthaloNH<sub>2</sub> molecules in DMSO (blue) and PBS (orange) solutions. The chemical structure of phthaloNH<sub>2</sub> can be found in inset (a). For both samples, the excitation wavelength was fixed at 745 nm. We used a concentration of 10<sup>-5</sup> M phthaloNH<sub>2</sub>.

## 2.2. PhthalonH<sub>2</sub> Loaded BSA NPs

### 2.2.1. Spectroscopic and Morphologic Characterization

As depicted in Figure 2a, the phthalonH<sub>2</sub> dispersed in BSA aqueous solution (green spectra) presents a broad absorption spectrum in the region of the NIR molecule, implying its mild degradation, while no meaningful fluorescence emission was noticed (Figure 2b). However, the BSA&phthalonH<sub>2</sub> NPs present, by comparison, a strong fluorescence intensity and a characteristic absorption spectrum (Figure 2a red spectrum), with a maximum at 762 nm and an emission maximum at 774 nm, confirming the formation of the BSA NPs and protection of the phthalonH<sub>2</sub> molecules within them. In accordance with Diac et al., the calculated relative fluorescence quantum yield of the newly synthesized BSA&phthalonH<sub>2</sub> NPs is  $\Phi = 17\%$  [31]. As standard reference, we used the fluorescence quantum yield of indocyanine green [32]. The second smaller maximum (701 nm) observed in Figure 2a can be assigned to a weak transition to the first excited state ( $S_0 \rightarrow S_1$ ), namely Q bands, attributed to the  $\pi-\pi^*$  transitions [33].

DLS and Zeta potential measurements of the recorded BSA&phthalonH<sub>2</sub> NPs, both at 25 °C and at 37 °C, suggest the promising potential of these protein-based NPs for translation to biomedical use, because they present a negatively charged surface ( $-12.6 \pm 0.9$  mV at 25 °C and  $-13.6 \pm 0.5$  mV at 37 °C) and a hydrodynamic diameter (Figure 3a) of  $28.54 \pm 0.42$  nm and PDI  $0.194 \pm 0.027$  at 25 °C (solid line) and  $25.06 \pm 0.62$  nm and PDI  $0.143 \pm 0.008$  at 37 °C (dashed line). The quite similar zeta potential (Figure S1 in Supplementary Materials) and diameter measured at 25 °C and 37 °C, respectively, underline the good stability and high potential of the BSA&phthalonH<sub>2</sub> NPs to be translated in biomedical applications, these values also being in the optimal range to benefit from the EPR effect. The TEM investigations presented in Figure 3b confirmed the size of the BSA NPs.

Moreover, even after 3 months of storage, the hydrodynamic diameter of the NPs is stable, as proven by DLS measurements (Figure S2a), while 71.4% of the initial fluorescence intensity is maintained (Figure S2b). The aspect of the BSA&phthalonH<sub>2</sub> NPs at the initial time and 3 months after the synthesis (Figure S2c) remains consistent, thus being additional proof that the BSA&phthalonH<sub>2</sub> NPs are stable upon storage. It is worth mentioning that the NPs were kept in storage at 4 °C and protected from light.

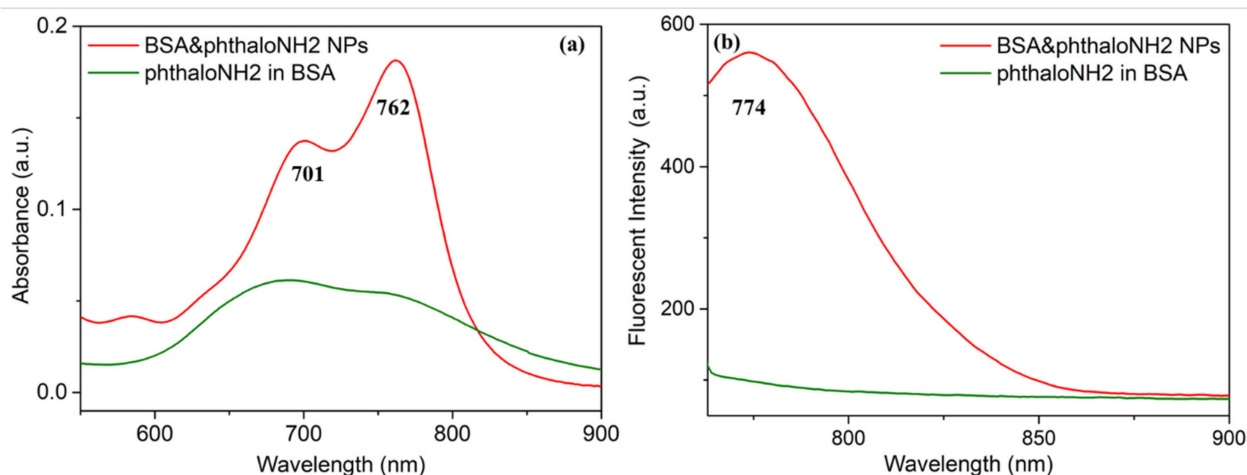


**Figure 2.** Absorbance (a) and fluorescence emission (b) spectra of the BSA&phthalonH<sub>2</sub> NPs (red) and phthalonH<sub>2</sub> in BSA solution (green). For both samples, the excitation wavelength was fixed at 745 nm. We used a concentration of  $10^{-5}$  M phthalonH<sub>2</sub>.

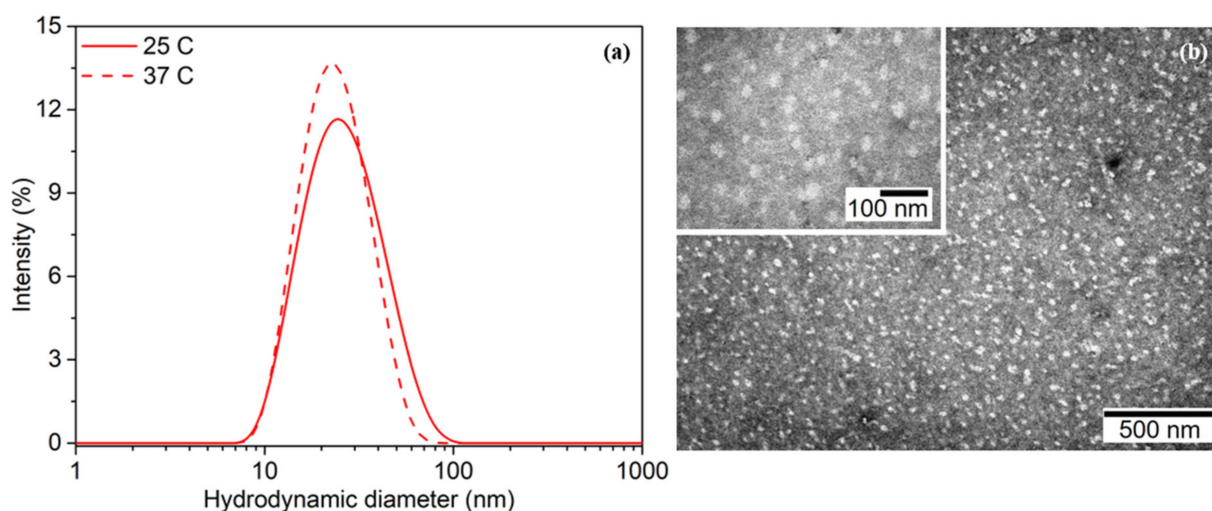


**Figure 3.** (a) DLS spectra of the BSA&phthalonNH<sub>2</sub> NPs at 25 °C (solid line) and at 37 °C (dashed line); (b) TEM images of the afresh synthesized BSA&phthalonNH<sub>2</sub> NPs.

### 2.2.2. BSA NPs Yield and phthalonNH<sub>2</sub> Loading Efficiency

Making use of the calibration curve (Figure S3a) calculated for different concentrations of BSA solutions, we determined the BSA&phthalonNH<sub>2</sub> NPs particle yield to be  $75.8 \pm 1.3\%$  by employing Equation (1). For absorbance measurements, the optical density of all samples was recorded at 277 nm. These results confirm the great reproductivity of our afresh designed BSA&phthalonNH<sub>2</sub> NPs, together with the tremendous formation rate of the particles. The loading efficiency of phthalonNH<sub>2</sub> was calculated using the previously established phthalonNH<sub>2</sub> calibration curve (Figure S3b) and Equation (2); the optical density of all samples was recorded at 774 nm. The obtained value,  $91.14 \pm 1.47\%$ , affirms the high amount of phthalonNH<sub>2</sub> confined within the BSA NPs and, undoubtedly, the excellent loading efficiency of our BSA&phthalonNH<sub>2</sub> NPs. Standard errors were calculated by triplicate analyses.

$$\text{Particle yield (\%)} = \frac{\text{BSA final quantity}}{\text{BSA initial quantity}} \times 100 \quad (1)$$

$$\text{Loading efficiency (\%)} = \frac{\text{Initial amount of phthalonNH}_2 - \text{Amount of phthalonNH}_2 \text{ in pellet}}{\text{Initial amount of phthalonNH}_2} \times 100 \quad (2)$$

Knowing the size of one molecule of BSA ( $14 \times 4 \times 4$  nm) and the volume of one BSA NP, we were able to determine the amount of BSA molecules per NP. Specifically, we calculated that in one NP we have 4074 BSA molecules. Then, we determined how many BSA NPs are in 1 mL of the final synthesis solution, using the following Equation (3):

$$C(M) = \frac{md}{M \cdot V_s} \quad (3)$$

where C(M)—molar concentration; md—BSA mass (g); V<sub>s</sub>—the solutions volume (L); and M—molar mass (g/mol).

Therefore, we obtain a number of  $845 \times 10^{14}$  BSA NPs in 1 mL of synthesis solution. Subsequently, using the same formula we determined a number of  $164.400 \times 10^{14}$  phthalonNH<sub>2</sub> molecules in 1 mL of solution.

Finally, using the following Equation (4), we achieved a number of 195 phthalonNH<sub>2</sub> molecules per one NP.

$$\frac{\text{Number of phthalonNH}_2 \text{ molecules}}{1 \text{ NP}} = \frac{\text{number of phthalonNH}_2 \text{ molecules in 1 mL}}{\text{number of NPs in 1 mL}} \quad (4)$$

### 2.2.3. Molecular Docking Simulation

Molecular docking is a useful tool in predicting the interactions that can take place between a ligand and a biomacromolecule. The molecular docking study was performed to obtain detailed information about how the phthalonNH<sub>2</sub> molecule binds to albumin, theoretically investigating the potential interactions between them.

Herein, the reason behind choosing the two molecular docking software applications was to obtain and compare the results generated by different algorithms and scoring functions; thus, the result of the *in silico* experiment can be better cross-validated. To obtain a more accurate and realistic result from the molecular docking study, on both software applications used we have changed some computational parameters such as *ga\_run*, *exhaustiveness*, and *num\_modes* to higher values compared to their default ones (and with our previous report [27]). The results of the molecular docking studies performed using AutoDock and AutoDock vina were evaluated in terms of the binding affinity of phthalonNH<sub>2</sub> to both Sudlow's binding sites, I and II, expressed as the variation of the Gibbs free energy ( $\Delta G$ ) and the resulting inhibition constant (Table 1). For the resulted conformations, the mean  $\Delta G$  and their standard deviation of the binding energies of the conformations were calculated and presented in Table 1. In addition, for both binding sites, using the built-in clustering function, the resulted 2 Å clusters of conformations of phthalonNH<sub>2</sub> given by AutoDock were presented in Table 1.

**Table 1.** The results of the docking study expressed as binding affinity of phthalonNH<sub>2</sub> to site I and site II of serum albumin expressed as variation of Gibbs free energy ( $\Delta G$ ), the computed inhibition constant (*K<sub>i</sub>*), and the analysis of clusters.

Sudlow's Sites	AutoDock					Autodock Vina				
	$\Delta G$ (kcal/mol)	<i>K<sub>i</sub></i> (nM)	Mean $\Delta G$ (kcal/mol)	$\Delta G$ SD	NC	Other Clusters		$\Delta G$ (kcal/mol)	Mean $\Delta G$ (kcal/mol)	$\Delta G$ SD
						NCoC	NoCl			
Site I	−10.79	12.23	−10.78	0.01	500	0	0	−10.10	−9.50	0.44
Site II	−8.80	352.01	−8.73	0.05	294	206	2	−9.00	−7.95	0.49

$\Delta G$ SD—standard deviation of the binding affinity of the resulted conformations; NC—number of conformations; NCoC—number of conformations found in other clusters; NoCl—number of other clusters.

The results of the molecular docking study performed with AutoDock indicate a good affinity of the compound phthalonNH<sub>2</sub> for binding site I compared to site II. This is quantified by the value of  $\Delta G = -10.79$  kcal/mol for binding site I, better than that for site II, where  $\Delta G = -8.80$  kcal/mol. Consequently, it brings a much lower *K<sub>i</sub>* value for site I (*K<sub>i</sub>* = 12.23 nM) than for site II (*K<sub>i</sub>* = 352.01 nM). Analyzing the dispersion of the binding energies of the generated conformations, we can observe that its average value in the case of site I,  $\Delta G = -10.78$  kcal/mol, is very close to the best ( $\Delta G = -10.79$  kcal/mol), with a small energy dispersion (SD = 0.01) between all generated conformations. The conformations predicted for phthalonNH<sub>2</sub> in site II have a slightly higher energy dispersion, the average value of  $\Delta G = -8.80$  kcal/mol, with a standard deviation equal to 0.05, slightly higher than in the case of site I. From a steric point of view, all conformations predicted of the phthalonNH<sub>2</sub> molecule in site I are found in a 2 Å cluster, much better than in the case of site II, where the conformation with the best binding has in its cluster 294 conformations out of the 500 generated. The other 206 conformations are found in another two 2 Å clusters.

The results of the molecular docking study performed with AutoDock vina show the same trend as in the case of the previous results presented, obtained using AutoDock. PhthalonNH<sub>2</sub> has a greater affinity for site I, rather than site II. This can be concluded by comparing its affinity for the two sites:  $\Delta G = -11.10$  kcal/mol for site I, and  $\Delta G = -9.00$  kcal/mol for site II, respectively. The energetic dispersion of the generated conformations indicates a high homogeneity of binding of phthalonNH<sub>2</sub> to site I, analyzing this by means of the average binding energy and the standard deviation. The standard deviations of the conformation's affinity are equal to 0.44 in the case of site I, while in the case of site II, it is slightly

higher, equal to 0.49. The comparative representation of the best conformations predicted by the two software applications used for the molecular docking is presented in Figure 4. It can be seen that phthaloNH<sub>2</sub> is positioned by both software applications in Sudlow's site I in almost the same position, while in the Sudlow's site II, they are significantly different.

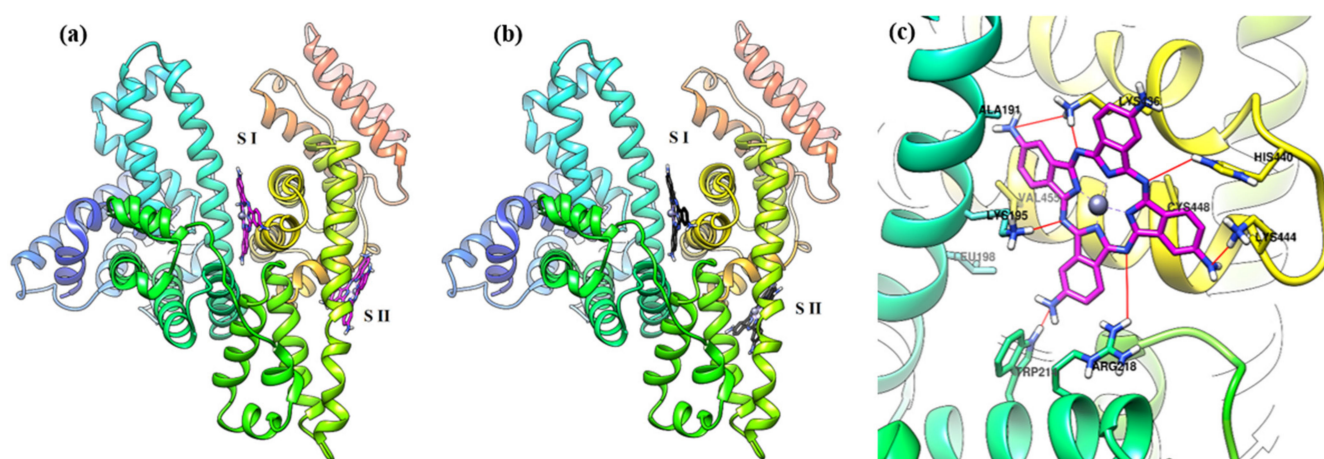


**Figure 4.** Graphic representation of the binding poses predicted for phthaloNH<sub>2</sub> into the two Sudlow's sites (S I and S II). The top conformations predicted by AutoDock are presented in the left side (a), with magenta colorization of the carbon atoms. The top conformations predicted by AutoDock vina are presented in the right side (b), with black colorization of the carbon atoms. The domains of albumin are colored the same between the two representations (a,b). The pose with the highest affinity of phthaloNH<sub>2</sub> into Sudlow's site I, with the depiction of interactions with the amino acid residues (c).

Figure 4c depicts the predicted interactions that can take place between phthaloNH<sub>2</sub> and the amino acids from albumin near Sudlow's binding site I. All four nitrogen atoms from phthaloNH<sub>2</sub> which connect the four isoindole units are predicted to interact with positively charged amino acid residues which surround the molecule (Lys195, Arg218, Lys436, and His440). Aromatic amines of phthaloNH<sub>2</sub> are predicted to interact with Trp214, Lys444, and Lys436. Of these amino acids, Arg218, Lys436, and Lys195 are reported in the literature to be important for the interaction of albumin with ligands [34,35]. As phthaloNH<sub>2</sub> is voluminous, it does not actually enter site I but is located in its vicinity, in the cleft found between subdomains IA and IIIA, as reported in the literature for the case of ligands with high molecular volume. PhthaloNH<sub>2</sub> has a rigid structure and is extended in two dimensions, compared to other compounds that have a longitudinally extended appearance and possibly have elements of flexibility, allowing them to bend. Analyzing other reports in the literature, in which albumin has been co-crystallized with longitudinal-looking ligands or having flexible elements, deep binding of phthaloNH<sub>2</sub> to Sudlow's site I is difficult due to its size and rigidity [36,37].

Considering Sudlow's site I as the main binding site of albumin, responsible for binding many drugs, and the preliminary docking results presented above, we will present a series of more detailed data from the molecular docking results of the compound at this site. Figure S4 shows the conformations with the highest affinity for site I, generated by the two software applications. It can be seen that they are almost overlapping. PhthaloNH<sub>2</sub> adopts a propeller-like conformation, possible due to its planes of symmetry.

Both AutoDock and AutoDock vina have yielded consistent results following exactly the same trends; thus, we can conclude that phthaloNH<sub>2</sub> binds well in site I of serum albumin, the conformations generated indicating that it binds homogeneously, taking into account the results from the energetic and steric perspective, as reported in the literature, as the main binding site of serum albumin for ligands. The contribution of site II in the binding of phthaloNH<sub>2</sub> can be taken into account, but with negligible influence, due to the much lower affinity of phthaloNH<sub>2</sub> to it and the dispersed conformations predicted into this site [38,39].

### 2.3. Free vs. Encapsulated PhthaloNH<sub>2</sub> within BSA NPs

#### 2.3.1. Temperature-Dependent Spectroscopic Characterization

Next, we wanted to compare the free phthaloNH<sub>2</sub> (blue spectra) with the previously synthesized BSA&phthaloNH<sub>2</sub> NPs (red spectra) at room temperature, 25 °C, and at a biologically relevant temperature, 37 °C, to confirm their adaptability in biomedical applications. In the absorbance (Figure 5a) and fluorescence emission (Figure 5b) spectra, we presented spectra measurements both at 25 °C and 37 °C. We can observe that the absorption and the emission maximum of BSA&phthaloNH<sub>2</sub> NPs does not shift once the temperature is increased, remaining preserved both at 25 °C (dashed line) and 37 °C (solid line). On the one hand, in the absorbance spectra (Figure 5a), free phthaloNH<sub>2</sub> has the exact same absorption maximum at 25 °C (dashed line) as at 37 °C (solid line), precisely 775 nm, but we can see a slight decrease in intensity as the temperature rises. On the other hand, in the fluorescence emission spectra, free phthaloNH<sub>2</sub> does not maintain its emission maximum constant. At 25 °C, it has an emission maximum at 796 nm (dashed line), but at 37 °C, the emission maximum shifts to smaller wavelengths at 795 nm (solid line). Additionally, we can remark that the free phthaloNH<sub>2</sub> does not lose its fluorescence emission intensity when the temperature rises. Moreover, the encapsulation of the phthaloNH<sub>2</sub> agent in the protein-based NPs is confirmed with the BSA&phthaloNH<sub>2</sub> NPs absorbance spectra change in the phthaloNH<sub>2</sub> specific region, leading to a hypsochromic shift of 13 nm. BSA&phthaloNH<sub>2</sub> NPs fluorescence emission undergoes changes compared to free phthaloNH<sub>2</sub> because of the environmental change from the photoactive agent immediately surrounding once encapsulated within the BSA NPs. There is a 22 nm blueshift between the free photoactive agent and the BSA&phthaloNH<sub>2</sub> NPs, proving once again that we successfully encapsulated the photoactive agent within the NPs.

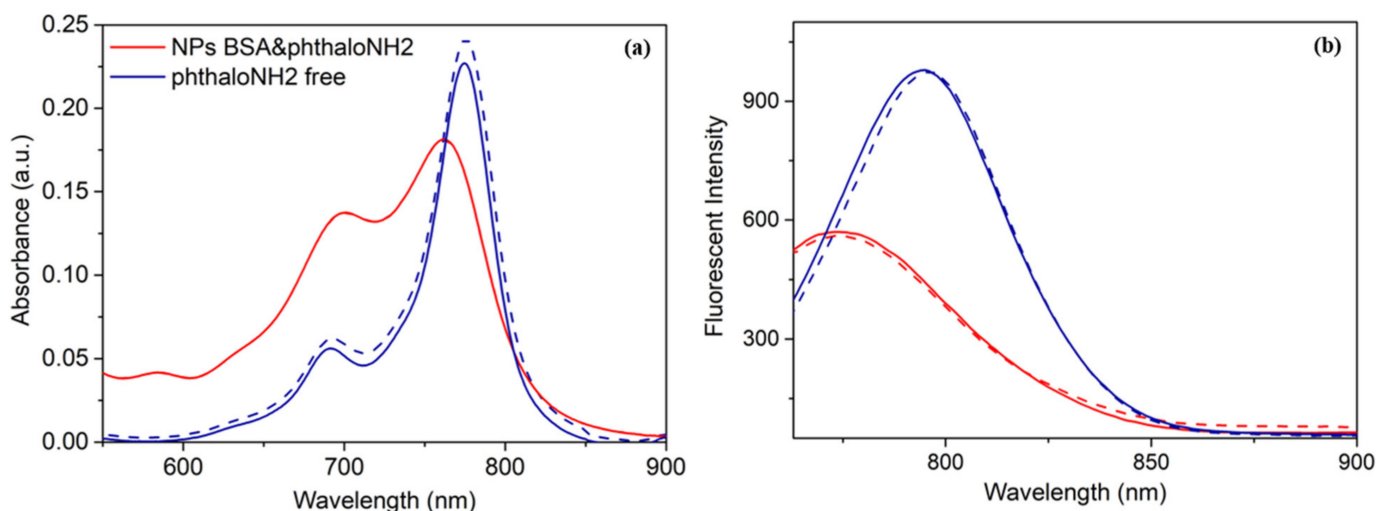


**Figure 5.** Absorption (a) and fluorescence emission (b) spectra recorded at 25 °C (dashed line) and at 37 °C (solid line) of the free photoactive agent (blue) compared with BSA&phthaloNH<sub>2</sub> NPs (red).

#### 2.3.2. MTT Assay

The MTT assay, the gold standard of the cell viability assay, has been the first step towards the translation of BSA&phthaloNH<sub>2</sub> NPs to pre-clinical studies. Thus, the A2780 ovarian cancer cell responses to free phthaloNH<sub>2</sub> and BSA&phthaloNH<sub>2</sub> NP treatments were analyzed after a 24 h incubation period. A concentration-dependent decrease in the number of viable cells was observed for the cells treated with the free phthaloNH<sub>2</sub> solution, and the IC<sub>50</sub> value was calculated to be 0.29 μM (Figure 6a). On the other hand, the treatment with BSA&phthaloNH<sub>2</sub> NPs led to no noteworthy variation in the viability of A2780 cancer cells, verifying their feasible utilization in biomedical applications. Furthermore, no cytotoxic effects were observed for the encapsulated phthaloNH<sub>2</sub> molecule,

even at concentrations 10 times higher than the IC<sub>50</sub> values of the free phthalonH<sub>2</sub> solution (Figure 6b), underlining once again the biocompatibility of the BSA NPs and the necessity to load the photosensitizer within them.

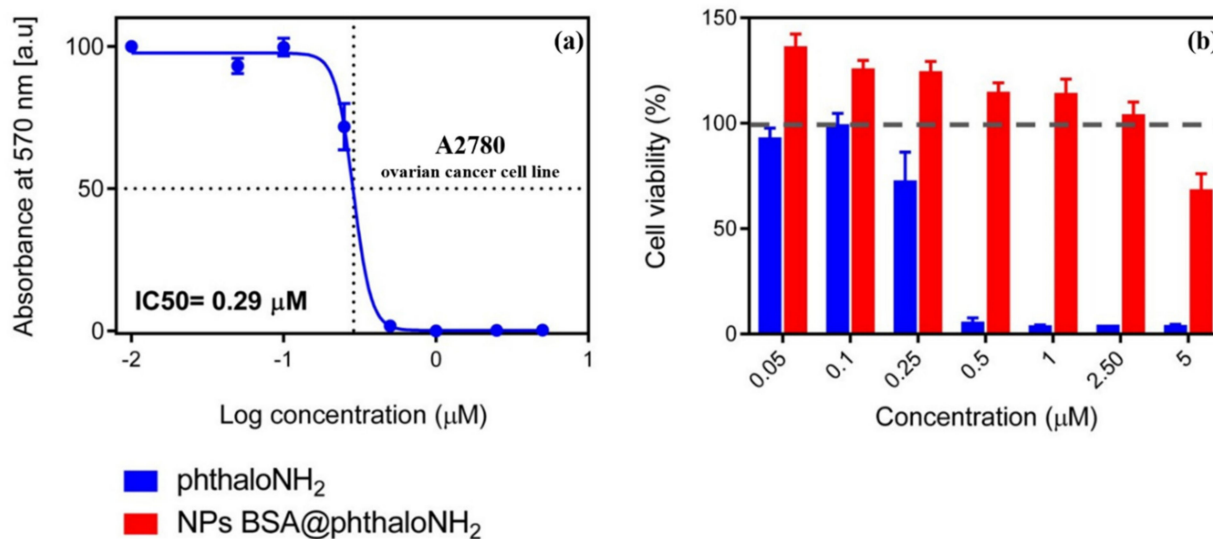
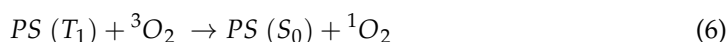
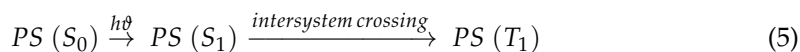


**Figure 6.** MTT cells assay; (a) survival curve of A2780 cells treated with phthalonH<sub>2</sub> —nonlinear regression; and four-parameter sigmoidal curve fit, each point representing mean  $\pm$  SEM in three separate measurements; dose-dependent decrease of the viability of A2780 cells treated with phthalonH<sub>2</sub>; (b) comparison of the viability of ovarian cancer cells treated with phthalonH<sub>2</sub> vs. BSA&phthalonH<sub>2</sub> NPs.

### 2.3.3. Photodynamic Effects

When irradiated, the PS molecule reaches the excited singlet state  $S_1$  due to photon absorption and returns to the ground state ( $S_0$ ) through various possible radiative (e.g., fluorescence) and non-radiative relaxation processes such as intersystem crossing to an excited triplet state level ( $T_1$ ) (Equation (5)). On the triplet state level, photochemical reactions are induced, which imply electron or hydrogen transfer. The PS reacts with  $^3O_2$  through energy transfer as the PS returns to the ground level and  $^1O_2$  is produced (Equation (6)), a strong cytotoxic agent in the PDT of cancers [40]. Hence, PDT efficiency depends on the yield of  $^1O_2$  generation but also on the nano-system ability to target the endorsed biological layer (for example, cancer cells) [4].



For this purpose, we studied the ABDA molecule in the presence of both BSA&phthalonH<sub>2</sub> NPs and free phthalonH<sub>2</sub> for the detection of  $^1O_2$ ; photo-induced degradation of ABDA occurs due to its interaction with the generated  $^1O_2$ . The evaluation principle of the photodynamic efficiency is based on the monitoring of ABDA degeneration throughout the irradiation period, the effect being recorded by a gradual decrease in intensity in the UV-vis absorbance region specific for ABDA.

To determine the efficiency to generate  $^1O_2$  of our BSA&phthalonH<sub>2</sub> NPs and free phthalonH<sub>2</sub>, we analyzed the degradation of ABDA by monitoring its absorbance spectra (Figure S5) in the UV region every 3 min after irradiating with a 785 nm laser for a total time of 15 min. The BSA&phthalonH<sub>2</sub> NPs caused some degradation of the ABDA molecule (Figure 7 red spectra) in the first 3 min of irradiation, while little changes were observed in the absorbance spectra of ABDA for the rest of the irradiation period, resulting in an  $^1O_2$  quantum yield of 0.06. On the other hand, a constant decrease in the ABDA

molecule amount was observed during the 15 min irradiation in the presence of the free phthalonNH<sub>2</sub> (Figure 7, blue spectra), resulting in an <sup>1</sup>O<sub>2</sub> quantum yield of 0.22. The discrepancies in the <sup>1</sup>O<sub>2</sub> quantum yield values determined for the two samples can be associated with the phthalonNH<sub>2</sub> molecule's rigid structure and possible hydrogen bridge formation once it binds within the BSA protein. In addition, closely related to the changes in the configuration of the molecules is another key property of PS agents, namely their intrinsic intersystem crossing rate. When encapsulated within the BSA protein, the dye is sheltered from the environment, and compared to the free phthalonNH<sub>2</sub> solution, the phthalonNH<sub>2</sub>-<sup>3</sup>O<sub>2</sub> interaction probability is lower. Another important factor in the dual behavior of phthalonNH<sub>2</sub> is the preferred solvent for each sample during the PDT assay, PBS for the BSA&phthalonNH<sub>2</sub> NPs and DMSO for the free phthalonNH<sub>2</sub>, considering the hydrophobicity of the dye and the degradation of the BSA NPs in DMSO. Control PBS and DMSO solutions were studied under identical conditions, but no indications of <sup>1</sup>O<sub>2</sub> generation were observed.

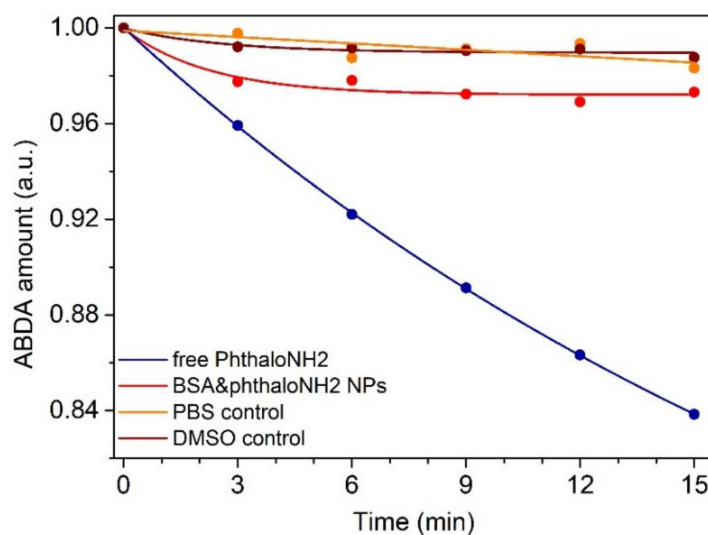


**Figure 7.** Degradation of ABDA molecule in the presence of free phthalonNH<sub>2</sub> (blue), BSA&phthalonNH<sub>2</sub> NPs (red), control PBS (orange), and DMSO (brown) solutions, monitored by modifications in the absorbance spectra of ABDA as a function of irradiation time.

#### 2.3.4. Photothermal Effects

To validate the protein-based NPs' potential as therapeutic agents in solution, we tested their capacity to convert light to heat and compared it with the one of the free phthalonNH<sub>2</sub> after irradiation with the same NIR laser, starting from 37 °C. The second non-radiative relaxation process relies on the internal conversion from the S<sub>1</sub> excited state in the form of heat and is known as the photothermal effect. The photothermal effect is described by the energy balance equation (Equation (7)); by analytically solving this equation, we can determine the temperature dissipated by the system to the surrounding environment (Equation (8)) [4].

$$\sum m_i C_i \frac{dT}{dt} = Q_0 - Q_{ext} \quad (7)$$

$$\Delta T = \tau \frac{Q_0}{\sum m_i C_i} (1 - e^{-\frac{t}{\tau}}) \quad (8)$$

Thus, to assess the efficiency of our fluorescent protein-based NPs to transform light to heat, as thermal agents in cancer therapy, we performed photothermal experiments on BSA&phthalonNH<sub>2</sub> NPs, free phthalonNH<sub>2</sub>, and control solutions such as PBS and DMSO for comparison. From Figure 8a,b, it can be observed that the BSA&phthalonNH<sub>2</sub> NPs heat up gradually, starting from an ambient temperature of 37 °C and reaching temper-

atures around 47 °C after just 15 min. These results confirm the promising potential of the BSA&phthalonH<sub>2</sub> NPs to be translate to pre-clinical studies, considering that their maximum temperature achieved is in the optimal temperature-time range for moderate-temperature hyperthermia [41].

Next, the photothermal conversion efficiency ( $\eta$ ) of the BSA&phthalonH<sub>2</sub> NPs was calculated to be 20%. The fact that these particles heat up with approximately 10 °C in such a short irradiation period and taking into account their great light-to-heat conversion performance, BSA&phthalonH<sub>2</sub> NPs show promising results in our search for obtaining NIR protein-based NPs with dual therapeutic effect. Compared to BSA&phthalonH<sub>2</sub> NPs, the free photoactive agent reaches a maximum temperature of 48.16 °C after the first 9 min of irradiation, but until minute 15, the temperature decreases to 46.87 °C. The free phthalonH<sub>2</sub> solution reaches slightly higher temperatures as the BSA&phthalonH<sub>2</sub> NPs because, once encapsulated, the photoactive molecule is protected within the protein, the heat transfer is lower, and it interacts less with the irradiation light. Nonetheless, the performance of the tested samples is determined based on the light-to-heat conversion efficiency. Thus, we can conclude that the BSA&phthalonH<sub>2</sub> NPs present better outcomes in comparison to the free phthalonH<sub>2</sub> solutions, the  $\eta$  for the free phthalonH<sub>2</sub> solution being 8.5%, once again underlining the benefit of encapsulating the NIR photoactive agent within BSA NPs. Contrary to the values of maximum temperature reached during the 15 min experiments, the light-to heat conversion efficiency is higher for the BSA&phthalonH<sub>2</sub> NPs due to the significant contribution of the absorption correction factor calculated for the optical density at the excitation wavelength (optical density at 785 nm for free phthalonH<sub>2</sub> solution: 0.08, and for BSA&phthalonH<sub>2</sub> NPs: 0.05) parameter present in the photothermal conversion efficiency equation (Equation (10), Section 4.8). Another key element in the discrepancy between the maximum temperature values and conversion efficiencies is the great difference in the specific heat capacity of the selected solvents; 1.97 J g<sup>-1</sup> K<sup>-1</sup> for DMSO (phthalonH<sub>2</sub>@DMSO) and 4.18 J g<sup>-1</sup> K<sup>-1</sup> for PBS (BSA&phthalonH<sub>2</sub> NPs@PBS). It is worth noting that the PBS and DMSO solutions are not photothermally active.

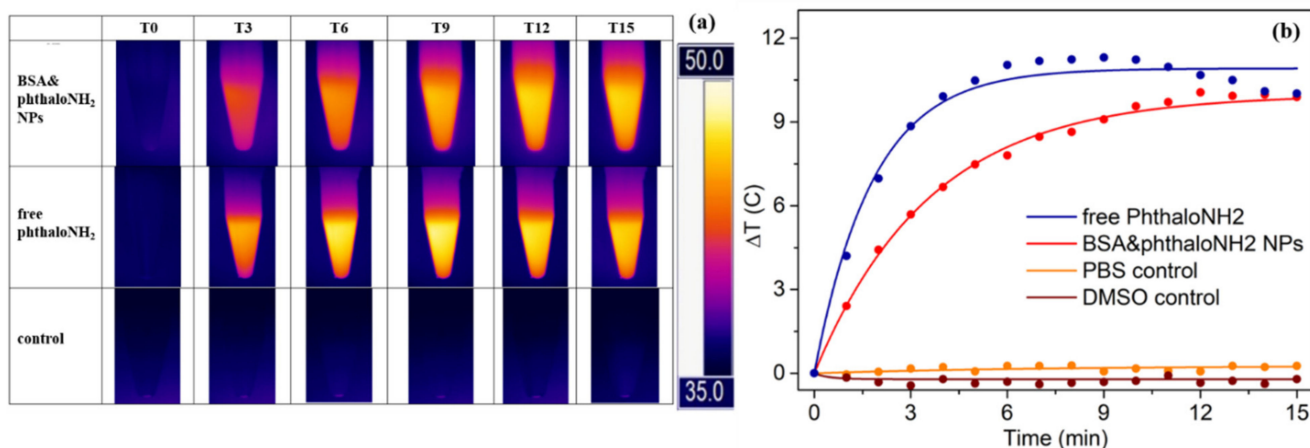


**Figure 8.** (a) Real-time photothermal images recorded under 785 nm laser irradiation through 15 min every 3 min of BSA&phthalonH<sub>2</sub> NPs, free phthalonH<sub>2</sub>, and PBS (as control); (b) Heating curves of free phthalonH<sub>2</sub> (blue), BSA&phthalonH<sub>2</sub> NPs (red), control PBS (orange), and DMSO (brown) solutions plotted against 15 min irradiation time.

### 2.3.5. Photothermal and Size Stability

Later on, to study the photothermal stability of the BSA&phthalonH<sub>2</sub> NPs and of the free phthalonH<sub>2</sub>, we exposed them to three successive heating and cooling down (On/Off) cycles. We exposed the samples to the laser for 15 min and then turned it off for another 15 min, allowing them to cool down to ambient temperature. As shown in Figure 9a, free phthalonH<sub>2</sub> (blue spectra) is able to convert light to heat faster, but after the first On/Off

cycle, thermal losses are observed. In the second cycle, the free photoactive agent heats up to 59.7% of the maximum temperature reached, while the NPs heat up to approximately the same temperature of 47 °C, precisely 91.45% of the maximum temperature recorded in the first cycle. In the last cycle, as also shown in Figure 9a, the maximum temperature of the free phthalonNH<sub>2</sub> was reduced by 55.8%, whereas for the BSA&phthalonNH<sub>2</sub> NPs, the maximum temperature was better maintained, being decreased by only 32.1%. This is another proof that we successfully encapsulated and protected the photoactive agent within the NPs.

Subsequently, we studied the BSA&phthalonNH<sub>2</sub> NPs' hydrodynamic diameter before and after irradiation. From Figure 9b, we observe that the BSA&phthalonNH<sub>2</sub> NPs decrease in intensity after irradiation, but the hydrodynamic diameter remains relatively constant. Before irradiation, the protein-based NPs have a hydrodynamic diameter of  $28.54 \pm 0.42$  nm and PDI  $0.194 \pm 0.027$ , and after exposure to the NIR laser line, they present a hydrodynamic diameter of  $30.66 \pm 1.30$  nm and PDI  $0.185 \pm 0.062$ , the insignificant 2 nm increase upholding the good size stability of our BSA&phthalonNH<sub>2</sub> NPs.

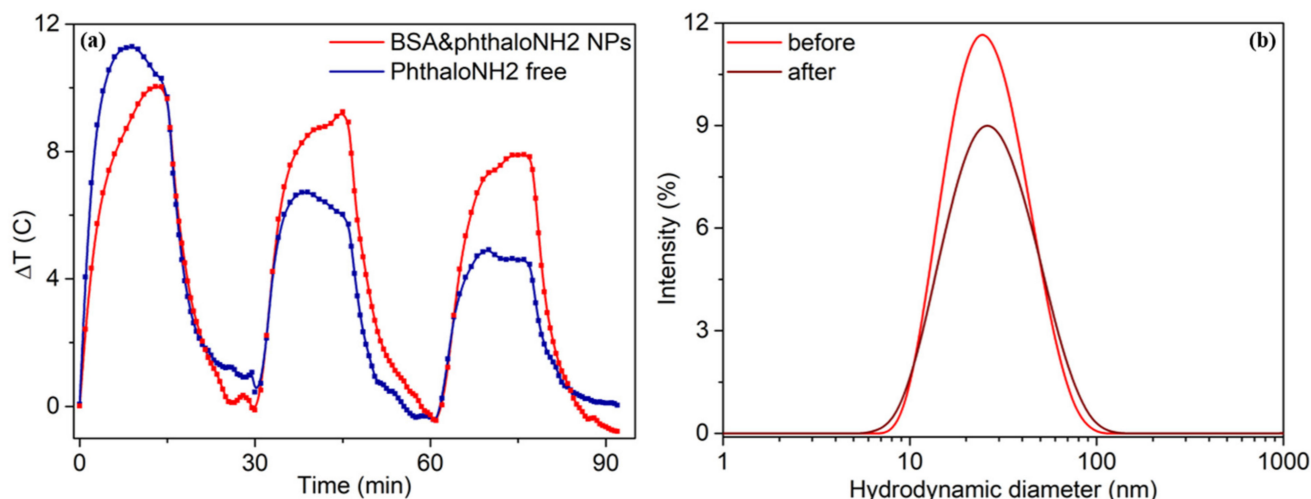


**Figure 9.** (a) The thermal curves of the BSA&phthalonNH<sub>2</sub> NPs (red) and of the free phthalonNH<sub>2</sub> (blue) obtained after three On/Off irradiation cycles. (b) The DLS spectra present BSA&phthalonNH<sub>2</sub> NPs' hydrodynamic diameter stability assay before (red) and after (brown) irradiation.

### 3. Discussion

To conclude, in this article, we successfully synthesized new and highly reproducible NIR albumin-based NPs as dual phototherapeutic agents, with versatile surface and great post-irradiation size stability NPs, having a diameter confirmed both by DLS and TEM images of  $25.06 \pm 0.62$  nm. The successful encapsulation of the free NIR photoactive agent within the NPs is confirmed both by molecular docking simulations, indicating the binding of the phthalonNH<sub>2</sub> molecule in site I of the albumin molecule, and also by the BSA&phthalonNH<sub>2</sub> NPs' absorbance spectra change in the phthalonNH<sub>2</sub> specific region. Furthermore, we demonstrated the NPs' stability at different temperatures, with a preserved absorption and emission both at 25 °C and 37 °C. We validated the BSA&phthalonNH<sub>2</sub> NPs' slight capacity to generate singlet oxygen by monitoring the degradation of the ABDA sensor under irradiation with a NIR 785 nm laser, resulting in a  $\Phi(^1\text{O}_2)$  of 0.06. The photothermal assay performed in the presence of the BSA&phthalonNH<sub>2</sub> NPs was a success, with an increase of 10 °C after only 15 min of irradiation with the 785 nm NIR laser, compared to the free phthalonNH<sub>2</sub>, which increases its temperature by 11 °C after 9 min of irradiation but then reaches a saturation point, and by the 15th minute of irradiation, its temperature is decreased by 2 °C. The BSA&phthalonNH<sub>2</sub> NPs present great photostability after 3 On/Off irradiation cycles (reaching 67.9% of the maximum

temperature recorded in the first cycle), compared to the free phthaloNH<sub>2</sub> which heats up only to 44.2% of the maximum temperature attained in the first cycle. To summarize, in this article, we reported the potential of our freshly synthesized BSA&phthaloNH<sub>2</sub> NPs to be translated in the future as therapeutic and fluorescent contrast agents in pre-clinical and clinical settings, by employing their great particle yield (over 75%), terrific encapsulation efficiency of phthaloNH<sub>2</sub> (over 91%), biocompatibility proven by the MTT assay, and surface capacity to be further functionalized for target delivery, alongside their dual photodynamic-photothermal therapeutic effects that could be implemented in the ongoing fight against cancer.

## 4. Materials and Methods

### 4.1. Materials

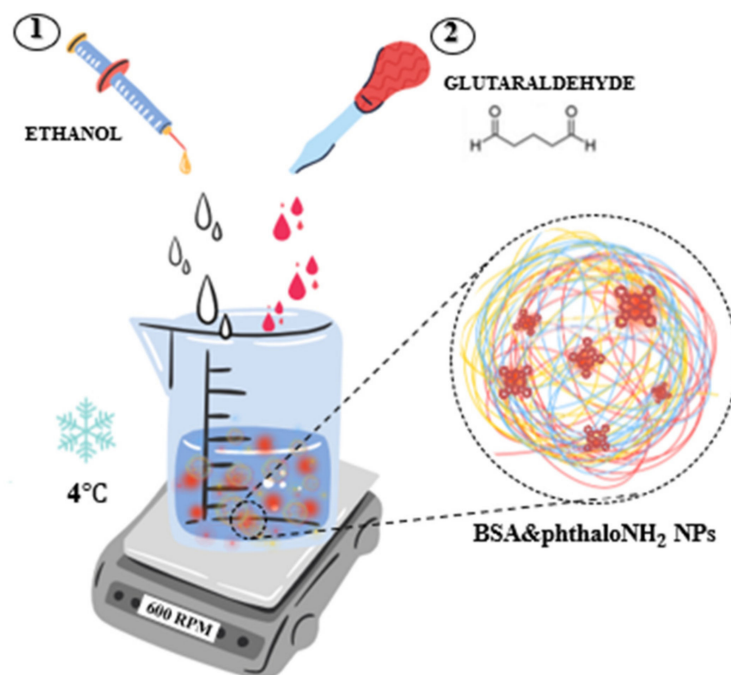
The materials used for this study are the following: bovine serum albumin; glutaraldehyde solution—grade I, 25% in water; 9,10-anthracenediyl-bis(methylene)dimalonic acid (ABDA); sodium sulfide nonahydrate (Na<sub>2</sub>S·9H<sub>2</sub>O); dimethylformamide (DMF); hydrochloric acid (HCl); sodium hydroxide (NaOH); RPMI medium, fetal calf serum (FCS); L-glutamine, penicillin-streptomycin solution; and [3-(4,5-dimethylthiazol-2-yl)-2,5-diphenyl-2H-tetrazolium bromide] (MTT). These were purchased from Sigma-Aldrich (Saint Louis, MO, USA) and used without any additional purification. Ethyl alcohol (EtOH) and dimethyl sulfoxide (DMSO) were purchased from Nordic Chemicals (Cluj-Napoca, Romania) and phosphate-buffered saline (PBS), without calcium or magnesium, was purchased from Lonza (Basel, Switzerland). We obtained ultrapure water from the Milli-Q purification system (Merck Millipore, Burlington, MA, USA), and we used it for all aqueous solution. The photoactive molecule of interest—phthaloNH<sub>2</sub>—was synthesized at the University of Chemistry, Cluj-Napoca, Romania (details in Section 4.2). For cell viability studies, A2780 ovarian cancer cell line from The European Collection of Authenticated Cell Cultures (ECACC), Porton Down Salisbury (Wiltshire, UK), was evaluated.

### 4.2. Synthesis of PhthaloNH<sub>2</sub>

The Zinc(II) tetranitrophthalocyanine (0.5 g × 0.6 mmol) and Na<sub>2</sub>S·9H<sub>2</sub>O (2 g, 8.3 mmol) were added to a 50 mL flask containing 10 mL DMF, stirred, and heated at 60–65 °C for 10 h, while the reaction progress was monitored by thin layer chromatography (TLC). The reaction mixture was cooled at room temperature, and after that, 10 g of crushed ice were added and stirred until melted. The solid was removed by filtration and was purified 3 times by mixing with 50 mL HCl 1M at 95 °C for 30 min. Then, it was filtered and washed with water until neutral pH. The solid was mixed with 50 mL NaOH at 90 °C for 30 min, filtered, washed with water until pH was neutral, and, finally, washed with ethanol, yielding 0.19 g (η = 50%) of dark greenish solid. MS (MALDI-TOF/TOF) *m/z*: 638.119 calculated for C<sub>32</sub>H<sub>20</sub>N<sub>12</sub>Zn, found 638.598 (Figure S6). FT-IR (KBr)  $\nu_{\max}/\text{cm}^{-1}$ : 3405, 1612, 1522, 1416, 1339, 1149, 1119, 1100, 1089, 1046, 848, 780, 757.

### 4.3. Design of BSA&phthaloNH<sub>2</sub> NPs

One major challenge presented in the literature in developing therapeutic agents is the synthesis of NPs with desired properties and functions. In many cases, the physical and chemical properties, such as the applicability of therapeutic NPs, are critically controlled by their size and surface chemistry, as well as the embedded photoactive molecule quantity. Thus, the first step of this study is focused on developing, in a controlled and reproducible manner, fluorescent protein-based NPs through loading the newly synthesized photoactive molecules with fluorescence emission in the NIR region, namely phthaloNH<sub>2</sub>. These NPs, being further referred to as BSA&phthaloNH<sub>2</sub> NPs, were synthesized on an ice bed after a modified and optimized synthesis protocol previously reported by our group [27] consisting of two steps: (i) desolvation using an organic solvent, ethanol, and (ii) stabilization by chemical cross-linking using glutaraldehyde (Scheme 1).



**Scheme 1.** The synthesis protocol of BSA&phthaloNH<sub>2</sub> NPs consisting of two steps: (i) desolvation and (ii) cross-linking.

We began by dissolving the BSA protein in water (5% concentration), having an adjusted pH of 8. Then, we obtained a solution based on EtOH and 100  $\mu\text{L}$  phthaloNH<sub>2</sub> stock solution, which was added in drops (1:1) over the BSA in water with a controlled speed of  $1 \text{ mL min}^{-1}$  using an automated syringe pump system, specifically NE-4000 Programmable Syringe from NEW ERA Pump systems Inc. (New York, NY, USA). The resulted solution was stirred during the entire preparation on a magnetic stirrer set at 600 RPM. After another 15 min, step 2 follows: the addition of glutaraldehyde as the stabilizer agent over the initial mixture, and finally, the solution was stirred for 24 h at a 4  $^{\circ}\text{C}$  temperature. The quantity of glutaraldehyde, in our case 40%, was relatively calculated as a function of the theoretical quantity needed for cross-linking all of the amino groups. The obtained NPs were firstly purified through a mechanic filter of 220 nm and then centrifuged for 1 h at room temperature, at 6000 RPM, in concentration tubes with a 100 kDa filtration membrane, to eliminate all remaining protein molecules after the NPs were formed. Subsequently, the solution was suspended in its initial volume in PBS. To eliminate the free dye excess, the NPs were centrifuged for 3 h at 18,000 RPM at room temperature in 1.5 mL centrifuge tubes. The supernatant was collected and stored for further use, while the pellet was suspended in DMSO and measured to determine the phthaloNH<sub>2</sub>'s loading efficiency in NPs.

#### 4.4. Particle Yield and Dye Loading Efficiency

To establish the particle yield and dye loading efficiency after the NPs were formed, we analyzed the final BSA and photoactive molecule concentration through monitoring the absorbance of the BSA&phthaloNH<sub>2</sub> NPs in the UV region for BSA (190–350 nm) and also in the NIR region for the phthaloNH<sub>2</sub> from the pellet (550–900 nm). In parallel, we measured the absorbance of different concentrations of BSA solutions, 1, 2, 3, 4, and 5%, and phthaloNH<sub>2</sub> resuspended in DMSO solutions,  $7.5 \times 10^{-7}$ ,  $10^{-6}$ ,  $2.5 \times 10^{-6}$ ,  $7.5 \times 10^{-6}$ ,  $10^{-5}$ , and  $2.5 \times 10^{-5}$  M, in order to create calibration curves.

#### 4.5. Molecular Docking

Serum albumin, a kind of globular protein from the family of albumins, can bind and transport a wide variety of substances in human plasma. It has multiple binding sites with different affinities for ligands, due to various hydrophobicity and spatial structure of the ligands and binding pockets [42]. The most common approach used in determining the ligand binding manner to proteins is the molecular docking study [43,44]. Next, we investigated the molecular mechanism of interaction between phthalonH<sub>2</sub> and serum albumin, taken from RCSB Protein Data Bank (entry code: 1AO6) [45,46]. The files of phthalonH<sub>2</sub> and macromolecules required for performing the molecular docking were prepared using the standard previously reported procedure using AutoDock Tools 1.5.6 and OpenBabel 2.3.2 [47–50].

The molecular docking of phthalonH<sub>2</sub> to serum albumin was carried out based on our group previous report using AutoDock 4.2.6 [49]. To have a clearer image about the molecular interactions that can take place between the phthalonH<sub>2</sub> and serum albumin, a supplementary molecular docking software, AutoDock vina 1.1.2, was used [51].

We have targeted in the molecular docking study the sites responsible for the carrier role of the protein, known as Sudlow's sites I and II, to determine the preferred site in which the compound binds. Both sites were found in the A fragment of the deposited homodimer structure. The present molecular docking study did not evaluate the binding of phthalonH<sub>2</sub> to another possible site: for example, at the surface of albumin macromolecules. As the albumin macromolecules were aggregated together in the process of synthesis of the nanoparticles, they have mutual influences, such deformations of steric hindrance on the external surfaces and pockets, making the molecular docking study unrealistic from this point of view. However, inclusion between two or more albumin macromolecules of a phthalonH<sub>2</sub> molecule may be possible but difficult to evaluate by molecular docking studies. The search space was configured for the docking procedure as specifically targeting the two pockets and avoiding blind docking [43]. The search space was configured as a cube, with coordinates of the center, as previously reported by our team [27]. In order to acquire more precise results, we changed some of the default or previously reported parameters in the molecular docking study. For AutoDock, the parameter *ga\_run* was set to 500, and for AutoDock vina, parameters *exhaustiveness* and *num\_modes* were set to 30 and 25, respectively. The conformations generated by AutoDock in both binding sites were grouped in clusters with relative root mean square deviation of 2 Å using the built-in function. The visualization of the docking results was performed using Chimera 1.10.2 [52].

#### 4.6. Cell Viability

At this point we focused on the viability of A2780 ovarian cancer cell line, in the presence of free phthalonH<sub>2</sub> and BSA&phthalonH<sub>2</sub> NPs. More specifically, the cells were kept in a humid incubator with 5% CO<sub>2</sub> at 37 °C in RPMI medium with 10% FCS, 1% glutamine, and 1% penicillin-streptomycin. A colorimetric cell viability assay, namely MTT, was used in order to assay the toxicity of free phthalonH<sub>2</sub> and BSA&phthalonH<sub>2</sub> NPs against A2780 cells. On 96-well plates, 20,000 cells/well were seeded and serial dilutions (0.05, 0.10, 0.25, 0.50, 1, 2.50, 5 µM) of both samples were added, while three wells were left without treatment, as control. Twenty-four hours later, the cellular media was changed, and MTT solution was added (100 µL, 1%). The cells were incubated for another hour until formazan crystals were formed, and 150 µL of DMSO was added to dissolve them. A Synergy 2 microplate reader from BioTek (Winooski, VT, USA) was used to measure the absorbance at 570 nm, and the surviving fraction was determined as the absorbance of the sample/absorbance of non-treated cells × 100. All experiments were executed in triplicate, and GraphPad Prism 6 software (San Diego, CA, USA) was implemented to process all data.

#### 4.7. Photodynamic and Photothermal Effects

The next step was the evaluation of the therapeutic potential of the BSA NPs loaded with photoactive molecules through testing the photoactive agents' capacity to generate singlet oxygen species ( $^1\text{O}_2$ ) in solution after irradiation with a NIR laser (Scheme 2), starting from the biologically relevant temperature of 37 °C.

Specifically, we started by measuring the UV-vis absorbance spectra (T0) of 500  $\mu\text{L}$  of sample in the presence of ABDA (0.3 mM) at 37 °C in a chamber. Then, we irradiated the sample with continuous-wave laser (i.e., laser diode with 785 nm wavelength of a Raman portable spectrometer R-3000CN, Raman Systems), at a power of 190 mW (0.93 W/cm<sup>2</sup> intensity) for 3 min and measured the absorbance spectrum again; these procedures were repeated 5 times. All UV-vis absorbance spectra were studied, and the intensity in the maximum point of the ABDA specific absorbance band located at 380 nm was recorded. In addition, control samples were tested under identical experimental conditions.

The PDT performance of the free phthalonNH<sub>2</sub> and BSA&phthalonNH<sub>2</sub> NPs was determined by calculating the singlet oxygen quantum yield using Equation (9) [4]:

$$\Phi(^1\text{O}_2) = \Phi(^1\text{O}_2)^{\text{MB}} * \frac{S * F^{\text{MB}}}{S^{\text{MB}} * F} \quad (9)$$

where  $\Phi(^1\text{O}_2)$ —the oxygen singlet quantum yield of the investigated sample;  $\Phi(^1\text{O}_2)^{\text{MB}}$ —the known quantum yield of the reference molecule (in our case, we used methylene blue (MB) as reference, whose  $\Phi(^1\text{O}_2)^{\text{MB}} = 0.52$  [4,52]); S—slope of the absorbance difference of ABDA in function of time for both sample and reference probe; and F—the absorption correction factor determined as  $F = 1 - 10^{-\text{OD}}$ , where OD is the optical density at the excitation wavelength, in our case at 785 nm.

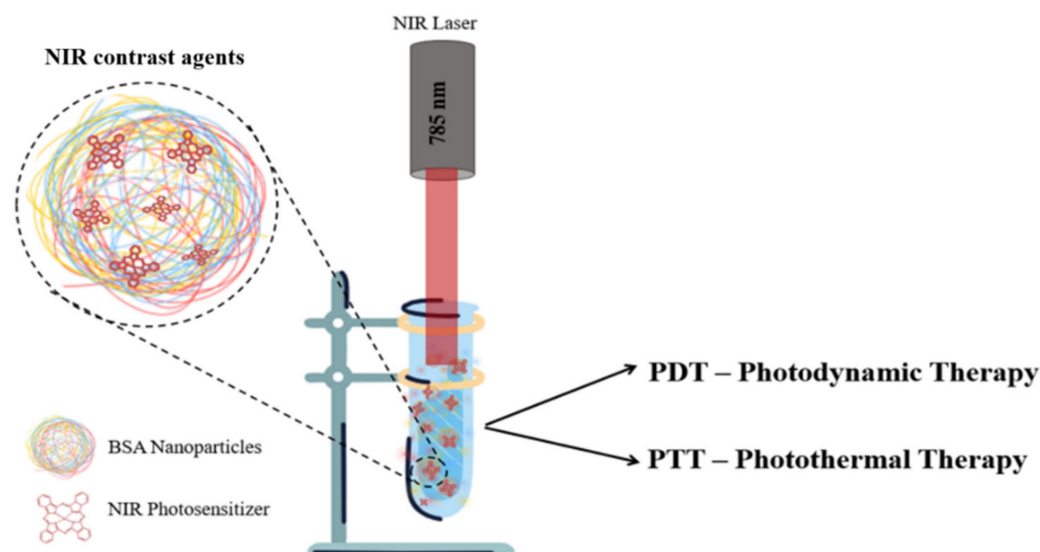
For the PTT evaluation, we maintained the same experimental setup and parameters as for PDT; 350  $\mu\text{L}$  of each sample was exposed continuously for 15 min to the 785 nm laser line, while every 30 s, we collected thermal images obtained with an IR camera with thermal vision, namely Optris PI 450 (Remscheid, Germany). After 15 min of irradiation, we turned off the laser and allowed the samples to cool down to ambient temperature. From the recorded thermal images, we extracted the temperature at every minute during the irradiation, thus determining the temperature increase relative to the ambient temperature. The photostability of the free phthalonNH<sub>2</sub> and BSA&phthalonNH<sub>2</sub> NPs was monitored during 3 On/Off cycles, while DLS measurements were recorded both before and after the irradiation to test their morphological stability.

To study the photothermic effect of the BSA&phthalonNH<sub>2</sub> NPs, we made DLS measurements both before and after irradiating them.

We determined the photothermal conversion efficiency ( $\eta$ ) for both the free phthalonNH<sub>2</sub> and BSA&phthalonNH<sub>2</sub> NPs using Equation (10) [4]:

$$\eta = \frac{h * A \Delta T - I \zeta}{I(1 - \zeta)(1 - 10^{-A_\lambda})} \quad (10)$$

where h—the heat transfer coefficient; A—the area cross section of irradiation;  $\Delta T$ —the temperature difference; I—the incident laser power;  $\zeta$ —the energy fraction absorbed by the cuvette and solvent; and  $A_\lambda$ —the absorbance of the probe at the excitation wavelength (more specifically, 785 nm).



**Scheme 2.** Illustration of the freshly synthesized NPs' potential operating as dual therapeutic agents upon irradiation with NIR laser.

#### 4.8. Characterization Techniques

Mass spectrometry was performed on a Rapiflex MALDI-TOF from Bruker Daltonics (Bremen, Germany) equipped with a Smartbeam 3D laser. FlexControl Version 4.0 from Bruker Daltonics was used to optimize and acquire data using the following parameters: positive ion polarity in reflectron mode, mass scan range ( $m/z$  100–1600), digitizer (5 GHz), detector voltage (2087 V), 1000 shots per pixel, and 10 kHz laser frequency. The laser power was set at 50% to 80% of the maximum, and 5000 laser shots were accumulated for each spectrum. The compound was dissolved in DMSO, and then a sample solution (1  $\mu$ L) was deposited onto the MALDI target, dried at room temperature, and analyzed in MALDI-TOF-MS using DHB (2,5-dihydroxybenzoic acid) without using MALDI matrix. Mass calibration of MALDI-TOF-MS was performed by the peptide mixture standard solution from Bruker Daltonics. TLC was performed on silica gel 60 F<sub>254</sub> aluminum sheets from Merck Millipore.

The FTIR spectra were recorded in KBr pastille using Alpha II spectrometer from Bruker Daltonics.

The UV-vis-NIR absorption spectra measurements were carried out with a Jasco V-670 UV-vis-NIR spectrophotometer procured from Jasco International Co., Ltd. (Tokyo, Japan) at a spectral resolution of 1 nm. The measurements were performed at room temperature as well as at 37 °C (relevant temperature from biological point of view) with the Peltier thermostatted single cell holder (air cooled), using quartz glass cuvettes (optical path of 2 mm) from Hellma (Müllheim, Germany).

The fluorescence emission measurements were performed by Jasco FP6500 spectrofluorometer from Jasco International Co., Ltd. (Tokyo, Japan). All measurements were performed at room temperature as well as at 37 °C with the Peltier thermostatted depolarization accessory (water-cooled), with a spectral resolution of 1 nm and a Xenon lamp as the excited source of 150 W. Emission spectra were obtained at a fixed excitation wavelength of 745 nm and 1  $\times$  10 nm excitation and emission bandwidths, using quartz glass cuvettes of 5  $\times$  5 mm from Hellma (Germany). The results have been recorded and analyzed using Spectra Manager program. We used the same concentration (herein 10<sup>-5</sup> M) of phthalonH<sub>2</sub> for both free phthalonH<sub>2</sub> and the loaded synthesized NP solutions.

Dynamic light scattering (DLS) and zeta potential measurements helped us to determine the hydrodynamic diameter and surface potential of the BSA&phthalonH<sub>2</sub> NPs. All measurements were made in triplicate using Zetasizer NanoZS90 equipment from Malvern Panalytical Ltd. (Worcestershire, UK) and using micro cuvettes for single use. In addition, for zeta potential measurements, we used a *dip cell* set (ZEN1002), and we applied a 5 V

voltage. The equipment has a He-Ne laser (633 nm, 5 mW), and all measurements were recorded at fixed temperatures of 25 °C and 37 °C.

Transmission electron microscopy (TEM) imaging was employed to determine the dry size of the BSA&phthaloNH<sub>2</sub> using a JEOL JEM-1010 microscope (Tokyo, Japan). The accelerating voltage was set at 30 kV, and the NPs were diluted in water (1:5000), dispersed on cellulose coated grids, and negatively stained by using uranyl acetate.

**Supplementary Materials:** The following are available online, Figure S1: Zeta potential measurements of the BSA&phthaloNH<sub>2</sub> NPs at 25 °C (solid line) and at 37 °C (dashed line), Figure S2: (a) DLS, (b) fluorescence, and (c) absorption spectra of the BSA&phthaloNH<sub>2</sub> NPs just after development (red) and after 3 months of storage (pink), Figure S3: The calibration curves for different concentrations of (a) free BSA (b) phthaloNH<sub>2</sub> dye solution, Figure S4: View from both sides of the poses predicted for phthaloNH<sub>2</sub> into the two Sudlow's site I by (a) AutoDock (carbon atoms in magenta) and (b) AutoDock vina (carbon atoms in black). Some amino acid labels were depicted for better comprehension, Figure S5: Degradation of ABDA during 15 min of irradiation in the presence of (a) BSA&phthaloNH<sub>2</sub> NPs and (b) free phthaloNH<sub>2</sub>, Figure S6: Mass spectra (MALDI-TOF/TOF): (a) the DHB (2,5-dihydroxybenzoic acid) matrix and (b) Zn (II)-2,9,16,23-tetraaminophthalocyanine (m/z = 638.578) in the presence of the DHB matrix.

**Author Contributions:** Conceptualization, M.F. and R.B.; methodology, M.F. and R.B.; software, G.M.; validation, R.B. and D.S.; investigation, R.B., D.S., A.C., D.M., L.G., M.P.-S. and M.S.; writing—original draft preparation, R.B. and D.S.; writing—review and editing, M.F. and S.A.; funding acquisition, S.A. All authors have read and agreed to the published version of the manuscript.

**Funding:** This work was supported by a grant from the Ministry of Research and Innovation, CNCS-UEFISCDI, project number PN-III-P4-ID-PCCF-2016-0142, within PNCD III. The present work has received financial support through the project: Entrepreneurship for innovation through doctoral and postdoctoral research, POCU/380/6/13/123886, co-financed by the European Social Fund, through the Operational Program for Human Capital 2014-2020.

**Data Availability Statement:** The data presented in this study are available on request from the corresponding author.

**Conflicts of Interest:** The authors declare no conflict of interest.

**Sample Availability:** Samples of the compounds are available from the authors.

## References

1. Bray, F.; Ferlay, J.; Soerjomataram, I.; Siegel, R.L.; Torre, L.A.; Jemal, A. Global Cancer Statistics 2018: GLOBOCAN Estimates of Incidence and Mortality Worldwide for 36 Cancers in 185 Countries. *CA Cancer J. Clin.* **2018**, *68*, 394–424. [[CrossRef](#)]
2. Thakor, A.S.; Gambhir, S.S. Nanoncology: The Future of Cancer Diagnosis and Therapy. *CA Cancer J. Clin.* **2013**, *63*, 395–418. [[CrossRef](#)]
3. Yao, C.; Zhang, L.; Wang, J.; He, Y.; Xin, J.; Wang, S.; Xu, H.; Zhang, Z. Gold Nanoparticle Mediated Phototherapy for Cancer. *J. Nanomater.* **2016**, *2016*, 5497136. [[CrossRef](#)]
4. Campu, A.; Focsan, M.; Lerouge, F.; Borlan, R.; Tie, L.; Rugina, D.; Astilean, S. ICG-Loaded Gold Nano-Bipyramids with NIR Activatable Dual PTT-PDT Therapeutic Potential in Melanoma Cells. *Colloids Surf. B Biointerfaces* **2020**, *194*, 111213. [[CrossRef](#)]
5. Baydoun, M.; Moralès, O.; Frochot, C.; Ludovic, C.; Leroux, B.; Thecua, E.; Ziane, L.; Grabarz, A.; Kumar, A.; de Schutter, C.; et al. Photodynamic Therapy Using a New Folate Receptor-Targeted Photosensitizer on Peritoneal Ovarian Cancer Cells Induces the Release of Extracellular Vesicles with Immunoactivating Properties. *J. Clin. Med.* **2020**, *9*, 1185. [[CrossRef](#)]
6. Champeau, M.; Vignoud, S.; Mortier, L.; Mordon, S. Photodynamic Therapy for Skin Cancer: How to Enhance Drug Penetration? *J. Photochem. Photobiol. B Biol.* **2019**, *197*, 111544. [[CrossRef](#)]
7. Gao, Y.; Li, Y. Gold Nanostructures for Cancer Imaging and Therapy. In *Advances in Nanotheranostics I*; Dai, Z., Ed.; Springer Series in Biomaterials Science and Engineering; Springer: Berlin, Germany, 2016; Volume 6, pp. 53–101. ISBN 978-3-662-48542-2.
8. Eskiizmir, G.; Baskin, Y.; Yapıcı, K. Graphene-based nanomaterials in cancer treatment and diagnosis. In *Fullerens, Graphenes and Nanotubes*; Elsevier: Amsterdam, The Netherlands, 2018; pp. 331–374. ISBN 978-0-12-813691-1.
9. Sheng, Z.; Cai, L. Organic Dye-Loaded Nanoparticles for Imaging-Guided Cancer Therapy. In *Advances in Nanotheranostics I*; Dai, Z., Ed.; Springer Series in Biomaterials Science and Engineering; Springer: Berlin, Germany, 2016; Volume 6, ISBN 978-3-662-48542-2.

10. Rajkumar, S.; Prabakaran, M. Multi-Functional FITC-Silica@gold Nanoparticles Conjugated with Guar Gum Succinate, Folic Acid and Doxorubicin for CT/Fluorescence Dual Imaging and Combined Chemo/PTT of Cancer. *Colloids Surf. B Biointerfaces* **2020**, *186*, 110701. [[CrossRef](#)]
11. Feng, J.; Chang, D.; Wang, Z.; Shen, B.; Yang, J.; Jiang, Y.; Ju, S.; He, N. A FITC-Doped Silica Coated Gold Nanocomposite for Both in Vivo X-Ray CT and Fluorescence Dual Modal Imaging. *RSC Adv.* **2014**, *4*, 51950–51959. [[CrossRef](#)]
12. Dreaden, E.C.; Alkilany, A.M.; Huang, X.; Murphy, C.J.; El-Sayed, M.A. The Golden Age: Gold Nanoparticles for Biomedicine. *Chem. Soc. Rev.* **2012**, *41*, 2740–2779. [[CrossRef](#)] [[PubMed](#)]
13. Oniszczyk, A.; Wojtunik-Kulesza, K.A.; Oniszczyk, T.; Kasprzak, K. The Potential of Photodynamic Therapy (PDT)—Experimental Investigations and Clinical Use. *Biomed. Pharmacother.* **2016**, *83*, 912–929. [[CrossRef](#)]
14. Van Leeuwen, F.W.B.; Hardwick, J.C.H.; van Erkel, A.R. Luminescence-Based Imaging Approaches in the Field of Interventional Molecular Imaging. *Radiology* **2015**, *276*, 12–29. [[CrossRef](#)]
15. Yu, J.; Zhang, X.; Hao, X.; Zhang, X.; Zhou, M.; Lee, C.-S.; Chen, X. Near-Infrared Fluorescence Imaging Using Organic Dye Nanoparticles. *Biomaterials* **2014**, *35*, 3356–3364. [[CrossRef](#)]
16. Ptaszek, M. Rational Design of Fluorophores for In Vivo Applications. In *Progress in Molecular Biology and Translational Science*; Elsevier: Amsterdam, The Netherlands, 2013; Volume 113, pp. 59–108. ISBN 978-0-12-386932-6.
17. Nalwa, H.S. (Ed.) *Supramolecular Photosensitive and Electroactive Materials*; Academic Press: San Diego, CA, USA, 2001; ISBN 978-0-12-513904-5.
18. Li, X.; Zheng, B.-D.; Peng, X.-H.; Li, S.-Z.; Ying, J.-W.; Zhao, Y.; Huang, J.-D.; Yoon, J. Phthalocyanines as Medicinal Photosensitizers: Developments in the Last Five Years. *Coord. Chem. Rev.* **2019**, *379*, 147–160. [[CrossRef](#)]
19. Wong, R.C.H.; Lo, P.-C.; Ng, D.K.P. Stimuli Responsive Phthalocyanine-Based Fluorescent Probes and Photosensitizers. *Coord. Chem. Rev.* **2019**, *379*, 30–46. [[CrossRef](#)]
20. Pereira, G.F.M.; Tasso, T.T. From Cuvette to Cells: How the Central Metal Ion Modulates the Properties of Phthalocyanines and Porphyrazines as Photosensitizers. *Inorg. Chim. Acta* **2021**, *519*, 120271. [[CrossRef](#)]
21. Teixeira Tasso, T.; Yamasaki, Y.; Furuyama, T.; Kobayashi, N. An Exemplary Relationship between the Extent of Cofacial Aggregation and Fluorescence Quantum Yield as Exhibited by Quaternized Amphiphilic Phthalocyanines. *Dalton Trans.* **2014**, *43*, 5886–5892. [[CrossRef](#)]
22. Sandra, F.; Khaliq, N.U.; Sunna, A.; Care, A. Developing Protein-Based Nanoparticles as Versatile Delivery Systems for Cancer Therapy and Imaging. *Nanomaterials* **2019**, *9*, 1329. [[CrossRef](#)] [[PubMed](#)]
23. Tarhini, M.; Greige-Gerges, H.; Elaissari, A. Protein-Based Nanoparticles: From Preparation to Encapsulation of Active Molecules. *Int. J. Pharm.* **2017**, *522*, 172–197. [[CrossRef](#)]
24. Pansare, V.J.; Hejazi, S.; Faenza, W.J.; Prud'homme, R.K. Review of Long-Wavelength Optical and NIR Imaging Materials: Contrast Agents, Fluorophores, and Multifunctional Nano Carriers. *Chem. Mater.* **2012**, *24*, 812–827. [[CrossRef](#)]
25. Madamsetty, V.S.; Mukherjee, A.; Mukherjee, S. Recent Trends of the Bio-Inspired Nanoparticles in Cancer Theranostics. *Front. Pharmacol.* **2019**, *10*, 1264. [[CrossRef](#)]
26. Gou, Y.; Miao, D.; Zhou, M.; Wang, L.; Zhou, H.; Su, G. Bio-Inspired Protein-Based Nanoformulations for Cancer Theranostics. *Front. Pharmacol.* **2018**, *9*, 421. [[CrossRef](#)]
27. Borlan, R.; Tatar, A.-S.; Soritau, O.; Maniu, D.; Marc, G.; Florea, A.; Focsan, M.; Astilean, S. Design of Fluorophore-Loaded Human Serum Albumin Nanoparticles for Specific Targeting of NIH:OVCAR3 Ovarian Cancer Cells. *Nanotechnology* **2020**, *31*, 315102. [[CrossRef](#)]
28. Cong, F.-D.; Ning, B.; Du, X.-G.; Ma, C.-Y.; Yu, H.-F.; Chen, B. Facile Synthesis, Characterization and Property Comparisons of Tetraaminometallophthalocyanines with and without Intramolecular Hydrogen Bonds. *Dye. Pigment.* **2005**, *66*, 149–154. [[CrossRef](#)]
29. Alzeer, J.; Roth, P.J.C.; Luedtke, N.W. An Efficient Two-Step Synthesis of Metal-Free Phthalocyanines Using a Zn(II) Template. *Chem. Commun.* **2009**, 1970. [[CrossRef](#)] [[PubMed](#)]
30. Borlan, R.; Focsan, M.; Perde-Schrepler, M.; Soritau, O.; Campu, A.; Gaina, L.; Pall, E.; Pop, B.; Baldasici, O.; Gherman, C.; et al. Antibody Functionalized Theranostic Protein Nanoparticles for Synergistic Deep Red Fluorescence Imaging and Multimodal Therapy of Ovarian Cancer. *Biomater. Sci.* **2021**. [[CrossRef](#)]
31. Diac, A.; Focsan, M.; Socaci, C.; Gabudean, A.-M.; Farcau, C.; Maniu, D.; Vasile, E.; Terec, A.; Veca, L.M.; Astilean, S. Covalent Conjugation of Carbon Dots with Rhodamine B and Assessment of Their Photophysical Properties. *RSC Adv.* **2015**, *5*, 77662–77669. [[CrossRef](#)]
32. Hong, N.Y.; Kim, H.R.; Lee, H.M.; Sohn, D.K.; Kim, K.G. Fluorescent Property of Indocyanine Green (ICG) Rubber Ring Using LED and Laser Light Sources. *Biomed. Opt. Express* **2016**, *7*, 1637. [[CrossRef](#)]
33. Sibata, M.N.; Tedesco, A.C.; Marchetti, J.M. Photophysicals and Photochemicals Studies of Zinc(II) Phthalocyanine in Long Time Circulation Micelles for Photodynamic Therapy Use. *Eur. J. Pharm. Sci.* **2004**, *23*, 131–138. [[CrossRef](#)] [[PubMed](#)]
34. Tayyab, S.; Sam, S.E.; Kabir, M.Z.; Ridzwan, N.F.W.; Mohamad, S.B. Molecular Interaction Study of an Anticancer Drug, Ponatinib with Human Serum Albumin Using Spectroscopic and Molecular Docking Methods. *Spectrochim. Acta Part A Mol. Biomol. Spectrosc.* **2019**, *214*, 199–206. [[CrossRef](#)]

35. Parsekar, S.U.; Velankanni, P.; Sridhar, S.; Halder, P.; Mate, N.A.; Banerjee, A.; Antharjanam, P.S.; Koley, A.P.; Kumar, M. Protein Binding Studies with Human Serum Albumin, Molecular Docking and in Vitro Cytotoxicity Studies Using HeLa Cervical Carcinoma Cells of Cu(II)/Zn(II) Complexes Containing a Carbohydrazone Ligand. *Dalton Trans.* **2020**, *49*, 2947–2965. [[CrossRef](#)]
36. Sakurama, K.; Kawai, A.; Tuan Giam Chuang, V.; Kanamori, Y.; Osa, M.; Taguchi, K.; Seo, H.; Maruyama, T.; Imoto, S.; Yamasaki, K.; et al. Analysis of the Binding of Aripiprazole to Human Serum Albumin: The Importance of a Chloro-Group in the Chemical Structure. *ACS Omega* **2018**, *3*, 13790–13797. [[CrossRef](#)]
37. Wang, Z.; Ho, J.X.; Ruble, J.R.; Rose, J.; Rümer, F.; Ellenburg, M.; Murphy, R.; Click, J.; Soistman, E.; Wilkerson, L.; et al. Structural Studies of Several Clinically Important Oncology Drugs in Complex with Human Serum Albumin. *Biochim. Biophys. Acta (BBA) Gen. Subj.* **2013**, *1830*, 5356–5374. [[CrossRef](#)] [[PubMed](#)]
38. Arfin, S.; Siddiqui, G.A.; Naem, A.; Moin, S. Inhibition of Advanced Glycation End Products by Isoferulic Acid and Its Free Radical Scavenging Capacity: An in Vitro and Molecular Docking Study. *Int. J. Biol. Macromol.* **2018**, *118*, 1479–1487. [[CrossRef](#)]
39. Balakrishnan, G.; Rajendran, T.; Murugan, K.S.; Ganesan, M.; Sivasubramanian, V.K.; Rajagopal, S. Synthesis, Photophysics and the Binding Studies of Rhenium(I) Diimine Surfactant Complexes with Serum Albumins: A Spectroscopic and Docking Study Approach. *J. Lumin.* **2019**, *205*, 51–60. [[CrossRef](#)]
40. Dougherty, T.J.; Gomer, C.J.; Henderson, B.W.; Jori, G.; Kessel, D.; Korbek, M.; Moan, J.; Peng, Q. Photodynamic Therapy. *JNCI J. Natl. Cancer Inst.* **1998**, *90*, 889–905. [[CrossRef](#)]
41. Habash, R.W.Y.; Bansal, R.; Krewski, D.; Alhafid, H.T. Thermal Therapy, Part 1: An Introduction to Thermal Therapy. *Crit. Rev. Biomed. Eng.* **2006**, *34*, 459–489. [[CrossRef](#)]
42. Zhang, J.; Gao, X.; Huang, J.; Wang, H. Probing the Interaction between Human Serum Albumin and 9-Hydroxyphenanthrene: A Spectroscopic and Molecular Docking Study. *ACS Omega* **2020**, *5*, 16833–16840. [[CrossRef](#)] [[PubMed](#)]
43. Nnyigide, O.S.; Lee, S.-G.; Hyun, K. In Silico Characterization of the Binding Modes of Surfactants with Bovine Serum Albumin. *Sci. Rep.* **2019**, *9*, 10643. [[CrossRef](#)]
44. Vieira, T.F.; Sousa, S.F. Comparing AutoDock and Vina in Ligand/Decoy Discrimination for Virtual Screening. *Appl. Sci.* **2019**, *9*, 4538. [[CrossRef](#)]
45. Berman, H.M.; Westbrook, J.; Feng, Z.; Gilliland, G.; Bhat, T.N.; Weissig, H.; Shindyalov, I.N.; Bourne, P.E. The Protein Data Bank. *Nucleic Acids Res.* **2000**, *28*, 235–242. [[CrossRef](#)]
46. Sugio, S.; Kashima, A.; Mochizuki, S.; Noda, M.; Kobayashi, K. Crystal Structure of Human Serum Albumin at 2.5 Å Resolution. *Protein Eng. Des. Sel.* **1999**, *12*, 439–446. [[CrossRef](#)]
47. O’Boyle, N.M.; Banck, M.; James, C.A.; Morley, C.; Vandermeersch, T.; Hutchison, G.R. Open Babel: An Open Chemical Toolbox. *J. Cheminform.* **2011**, *3*, 33. [[CrossRef](#)] [[PubMed](#)]
48. Stoica, C.I.; Marc, G.; Pirnău, A.; Vlase, L.; Araniciu, C.; Oniga, S.; Palage, M.; Oniga, O. Thiazolyl-Oxadiazole Derivatives Targeting Lanosterol 14 $\alpha$ -Demethylase as Potential Antifungal Agents: Design, Synthesis and Molecular Docking Studies. *Farmacia* **2016**, *64*, 390–397.
49. Morris, G.M.; Huey, R.; Lindstrom, W.; Sanner, M.F.; Belew, R.K.; Goodsell, D.S.; Olson, A.J. AutoDock4 and AutoDockTools4: Automated Docking with Selective Receptor Flexibility. *J. Comput. Chem.* **2010**, *30*, 2785–2791. [[CrossRef](#)] [[PubMed](#)]
50. Trott, O.; Olson, A.J. AutoDock Vina: Improving the Speed and Accuracy of Docking with a New Scoring Function, Efficient Optimization, and Multithreading. *J. Comput. Chem.* **2010**, *31*, 455–461. [[CrossRef](#)] [[PubMed](#)]
51. Pettersen, E.F.; Goddard, T.D.; Huang, C.C.; Couch, G.S.; Greenblatt, D.M.; Meng, E.C.; Ferrin, T.E. UCSF Chimera—A Visualization System for Exploratory Research and Analysis. *J. Comput. Chem.* **2004**, *25*, 1605–1612. [[CrossRef](#)] [[PubMed](#)]
52. Adarsh, N.; Avirah, R.R.; Ramaiah, D. Tuning Photosensitized Singlet Oxygen Generation Efficiency of Novel Aza-BODIPY Dyes. *Org. Lett.* **2010**, *12*, 5720–5723. [[CrossRef](#)] [[PubMed](#)]